Impact of downward longwave radiative deficits on Antarctic sea-ice extent predictability during the sea ice growth period

Ivana Cerovečki, Rui Sun, David H. Bromwich, Xun Zou,
Matthew R Mazloff, Sheng-Hung Wang

Appendix

1.   Regional model setups (Fig. S1)

The ocean model domain and bathymetry, based on ETOPO 2' bathymetry, are shown in Fig. 1. The MITgcm is implemented using a horizontal grid with 960×960 points (the grid spacing of approximately 10 km) and a polar stereographic projection, to match the atmospheric Polar WRF in the coupled system. The domain is centered at the South Pole and the true latitude is 70°S (the grid spacing is 10 km near the true latitude and is slightly different near the pole and the equatorial regions due to the map projection effect). The domain encompasses the area with latitudes higher than 48°S and the corners of the domain reach 32°S. There are 52 levels in the vertical direction that are more closely spaced in the oceanic mixed layer. The model resolution is similar or higher than those used in the S2S forecasts database, ensuring that all the processes resolved in the current S2S efforts are resolved in the MITgcm model. The uncoupled MITgcm model uses the surface forcing from ERA5 reanalysis, including surface radiative fluxes, surface wind speed, and freshwater flux. In MITgcm, the surface turbulent fluxes are estimated using the Large and Yeager (2009) bulk formulae. The thermodynamics of the MITgcm sea ice model are based on the zero-layer approximation of Semtner (1976), with numerous important modifications (Fenty and Heimbach 2013), while the MITgcm sea ice dynamical model is evolved from Hibler (1979) as discussed in Losch *et al* (2010).

The coupled regional model used in this work builds on the Scripps–KAUST Regional Integrated Prediction System (SKRIPS, Sun *et al* 2019). It is comprised of Polar WRF model for the Southern Ocean atmosphere (e.g., Bromwich et al, 2013; Deb *et al* 2016, 2018) that is coupled to the MITgcm ocean and sea ice model component using the Earth System Modeling Framework (ESMF) coupler. In the coupling process, the MITgcm sends the sea surface temperature (SST), ocean surface velocity, and sea ice fraction to ESMF, and ESMF sends them to Polar WRF as the bottom boundary conditions. Polar WRF sends surface fields to ESMF, including downward longwave and shortwave radiative fluxes, 10-m wind speed, precipitation, and evaporation. Polar WRF was run with a 20 km grid spacing and 71 vertical levels, the lowest being at 4 m. The model atmospheric physical parameterizations are the same as used by Hines *et al* (2019) with the cloud microphysics scheme from Morrison *et al* (2005) being applied.

In this work, we perform a series of dynamical downscale hindcasts using the MITgcm model and the coupled model. The MITgcm regional model uses the assimilated HYCOM/NCODA 1/12°

daily global analysis data (the Global Ocean Forecast System, Version 3.0, https://www.hycom.org/dataserver/gofs-3pt0/analysis, Chassignet *et al* 2007) as initial and boundary conditions for ocean temperature, salinity, and horizontal velocities. The ocean boundary conditions are obtained by linear interpolation of the weekly HYCOM/NCODA analysis data. They have been applied as a relaxation term at the lateral boundaries, over a restoring layer with a width of 13 grid cells. The relaxation timescales at the inner and outer boundary of the restoring layer are 10 and 0.5 days, respectively. The atmospheric model uses ERA5 as its initial and boundary conditions. For the atmospheric model, the boundary condition applied to the outer-most grid of our computational domain, which is referred to as the 'specified' zone in WRF, is obtained by linear interpolation of the 6 hourly ERA5 data. This linearly interpolated boundary condition is further 'relaxed' within the WRF 'relaxation' zone as a relaxation term. This way the simulation results from the model are 'relaxed' toward the boundary condition value. Here we use the default width of one grid point for the specified zone and four grid points for the relaxation zone. More details on the 'specified' zone and 'relaxation' zone can be found in the WRF tutorials. The spectral nudging was used in WRF to constrain the atmospheric potential temperature, wind speed, and water vapor mixing ratio between the planetary boundary layer (PBL) to the top of the model. The nudging was performed for wavenumbers < 11 in both directions, which corresponds to nudging towards wavelengths longer than about 800 km. The spectral nudging was not applied in the PBL.

(a) MITgcm model

Forced by ERA5
shortwave radiation
longwave radiation
2-m air temperature
2-m air humidity
10-m wind speed
precipitation

MITgcm
ocean model

(b) coupled model

longwave radiation
shortwave radiation
2-m air temperature
2-m air humidity

10-m wind speed
precipitation
evaporation

ESMF/NUOPC coupler

MITgcm–ESMF interface

SST current
sea-ice

WRF–ESMF interface

MITgcm
ocean model
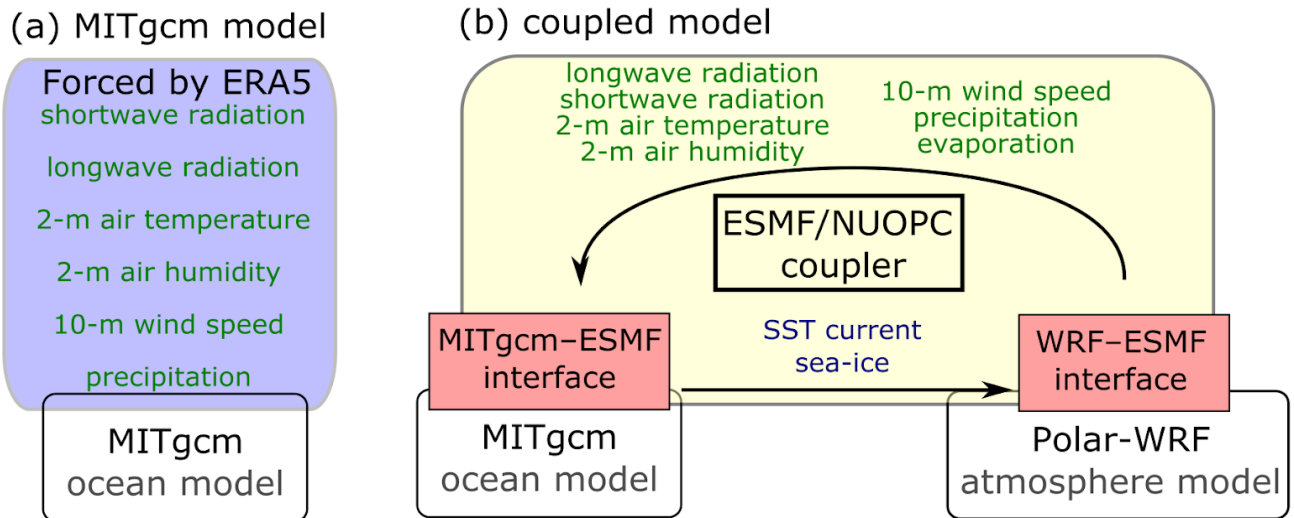
Polar-WRF
atmosphere model

Fig. S1. Schematic diagrams of (a) the MITgcm ocean model and (b) the coupled model used in this work.

2. Difference between ERA5 and BSRN at Neumayer and Syowa

Over the vast Antarctic continent, high-quality surface observations are limited. To fill this gap, the World Climate Research Programme (WCRP) initiated the Baseline Surface Radiation Network (BSRN) that provides quality-controlled observations of the surface radiation budget for climate research (Driemel *et al* 2018). There are only four BSRN stations that offer 1-minute temporal resolution data on both basic meteorological variables and radiative parameters over Antarctica, and Syowa and Neumayer are located in the area of interest (Fig. 1). With regular cleaning and maintenance by the permanent staff, the accuracy of DLW measurements at these stations is 2% or 3 Wm^{-2} based on BSRN standards (e.g., McArthur 2005). Also, BSRN observations have been widely used in previous research for model evaluation purposes and are proven to be the highest quality in-situ data (e.g., Wang and Dickinson 2013). Thus, to examine the potential negative bias of DLW in ERA5 for coastal Antarctica, this study uses BSRN observations from Neumayer and Syowa as the reference (https://bsrn.awi.de/).

Fig. S2 shows the box plot for monthly difference of DLW between ERA5 reanalysis data and BSRN observations at Neumayer and Syowa during 2018 and 2016 - 2020 periods. BSRN observations are first converted into daily averages and then compared with ERA5 on a monthly basis. In May 2018, the daily bias of DLW was between 20 to -70 Wm^{-2} at Syowa and between 18 to -60 Wm^{-2} at Neumayer, both with a daily mean bias of -8 Wm^{-2} (Figs. S2a and S2b). For monthly analysis during 2016 - 2020 period, ERA5 shows a negative bias in DLW with negative monthly bias between -2 and -19 Wm^{-2} and varying between different months. The negative bias in ERA5 maximizes during austral summer (DJF) and minimizes around August. In general, ERA5 tends to slightly underestimate the DLW along the coast of Antarctica. The magnitude of this underestimation is conjectured to increase over the ocean area that is away from the coast and impacted much more frequently by oceanic air masses.

3. The modeled sea ice growth in May 2016 and 2017

To confirm the generality of the analysis for the year 2018, we have additionally analyzed the sea ice growth in May 2016 and 2017 simulated by the MITgcm model. It can be seen in Fig. S3 that the ocean-sea ice model over-estimated the sea-ice evolution in both 2016 and 2017 compared with NSIDC data. The evolution of the sea-ice extent area is also shown in Figs. S4 and S5. When we artificially increase the longwave radiation by 50 Wm^{-2} in the simulation, the results obtained from the MITgcm model agree much better compared with the NSIDC data. By showing the sea-ice evolution simulated in other years, we show that the ocean model consistently overestimates sea ice growth every winter.
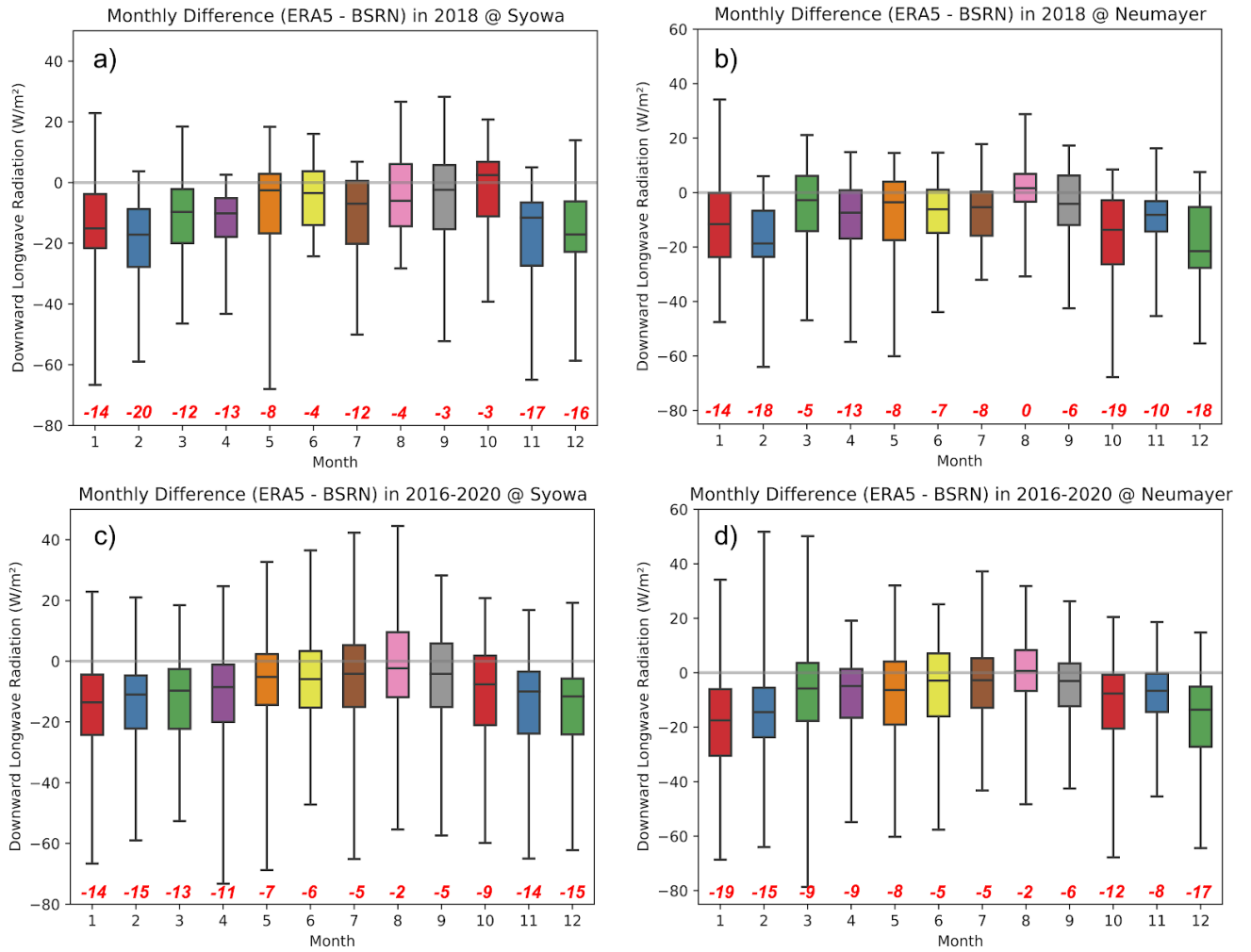
Fig. S2. Box plot for monthly difference between BSRN stations (Syowa and Neumayer) and ERA5 reanalysis data for 2018 and 5-year average (2016 - 2020). The red numbers are the average monthly difference. The gray line is the reference for 0 Wm^{-2}.
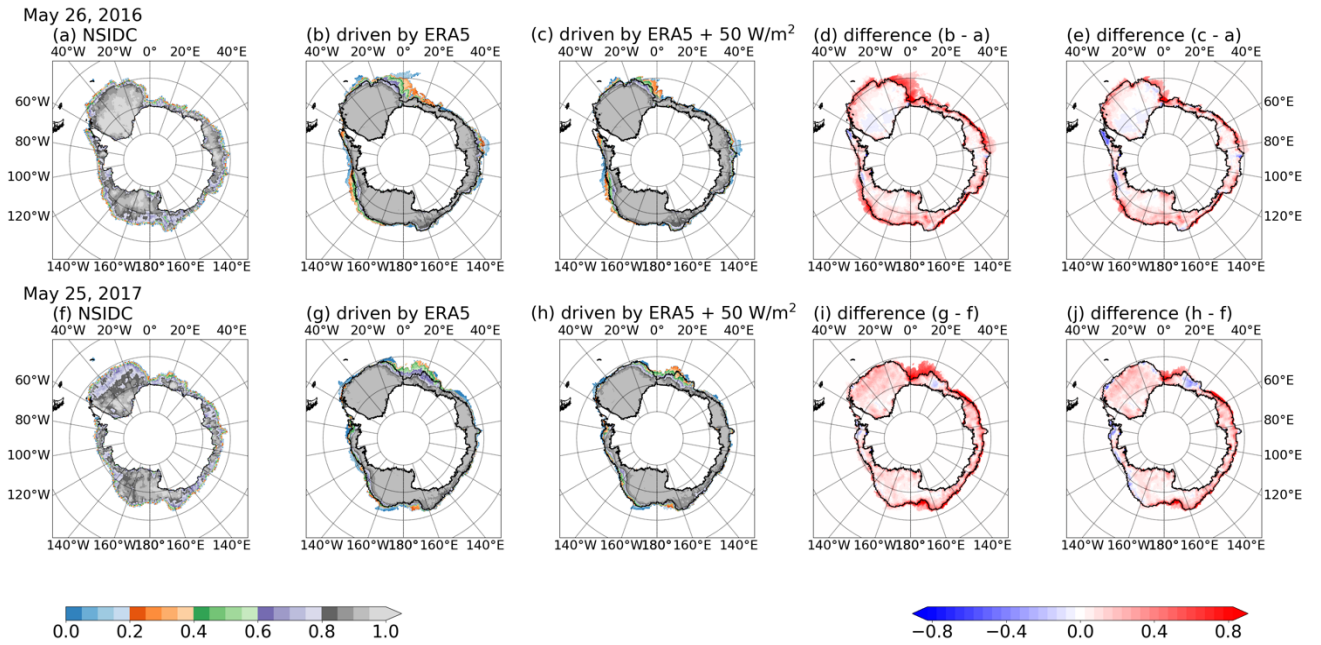
Fig. S3. Snapshots of sea-ice fraction from on 26 May 2016 and 25 May 2017. Panel (a) and (f) are the NSIDC data; (b) and (g) are the simulation results from uncoupled model driven by ERA5; (c) and (h) are the simulation results driven by ERA5 with an artificial increase of DLW radiation by 50 Wm^{-2}. Panel (d), (e), (i), and (j) are the differences between the simulations with NSIDC data. The black contours indicate the sea-ice extent (15% sea-ice concentration) from NSIDC data.

4. The net surface heat fluxes in MITgcm

To test the sensitivity of sea ice evolution in the MITgcm ocean model, we artificially increase the longwave radiation by 50 Wm^{-2} to the south of 60°S. To illustrate the impact of the artificially increased longwave radiation, the net surface heat flux Q_{net} is shown in Fig. S6. The Q_{net} in the two runs is similar north of 60°S, while the difference between Q_{net} is about 50 Wm^{-2} in the open water south of 60°S (Fig. S6). Because the sea-ice extent areas are different between the two runs driven by different heat fluxes, when there is less sea-ice, the ocean evaporates more and loses more heat, showing negative Q_{net} in Fig. S6c.
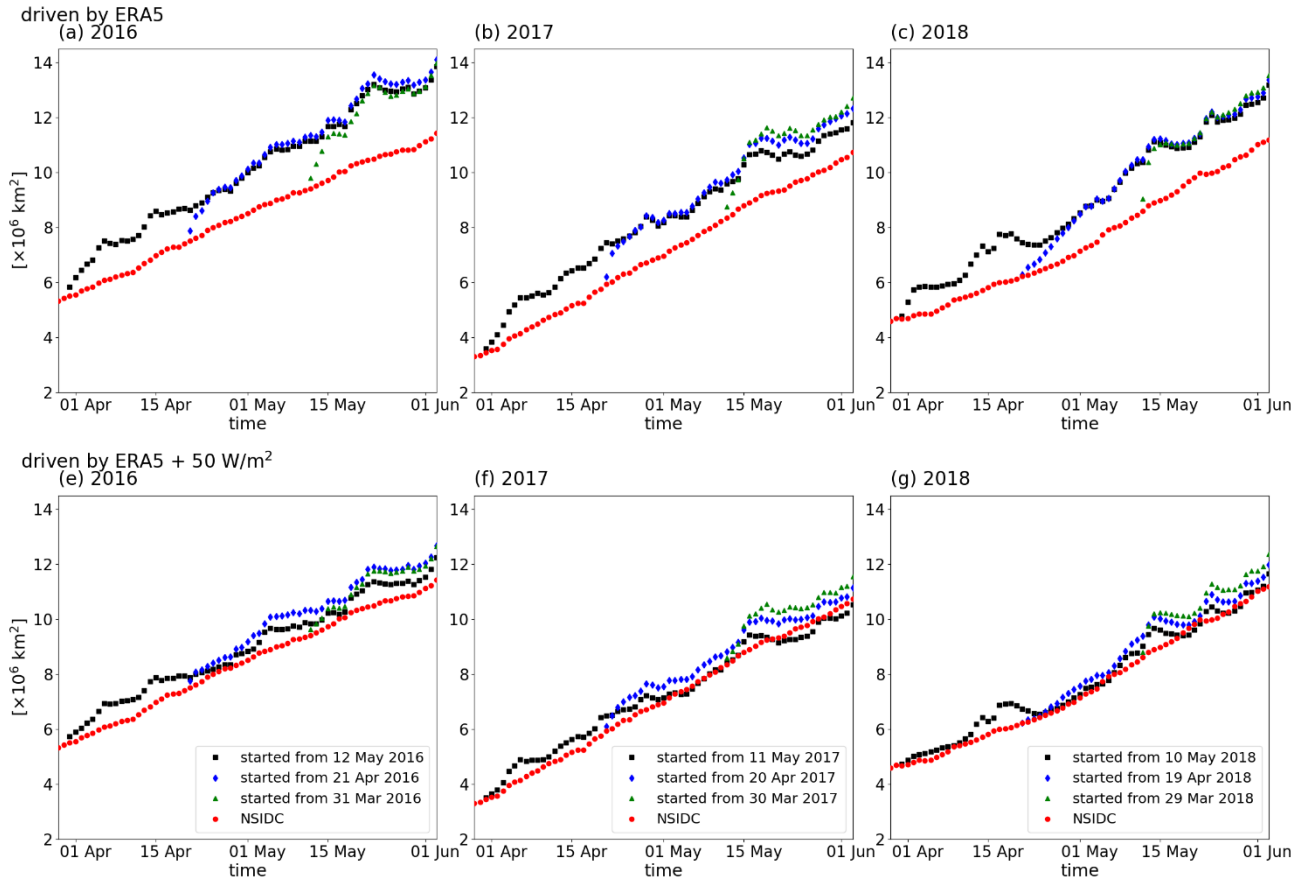
Fig. S4. Illustration of the sea-ice growth in 2016, 2017, and 2018, showing the circumpolar sea-ice extent area obtained in MITgcm model. Panels (a-c) show the simulation results in 2016-2018 driven by ERA5; Panels (d-f) show the simulation results in 2016-2018 driven by ERA5, but with an artificial increase of downward longwave radiation by 50 Wm^{-2}.

5. The model sea ice growth sensitivity to the lead closing parameter, vertical mixing of the ocean and of sea-ice extent definition

We first examine the sensitivity of the sea-ice growth to the lead closing parameter h_0 (parameter HO in MITgcm, which has a default value of 0.5 meters), which determines the initial vertical and horizontal proportion of sea ice growth. Varying h_0 between 0.05m and 1 m shows that the sea ice growth is not very sensitive to this selection (Fig. S7a). In all cases the sea ice grew too fast compared to the observations (Fig. S7a). We also tested the vertical diffusion coefficient Kv in ocean model component. Although vertical mixing plays an important role in governing the upper ocean heat content, the sea ice growth was not sensitive to changes in vertical mixing coefficient ($Kv=10^{-3}$, 10^{-4} and 10^{-5} m^2/s), unless we use a vertical diffusivity coefficient of $Kv=10^{-2}$ m^2/s (Fig. S7b). While $Kv=10^{-2}$ m^2/s is expected during episodic storm events, it is unphysical to use this value as a constant background turbulence level for the entire simulation, suggesting that potential errors in ocean mixing are not the dominant cause for the excess sea ice growth.
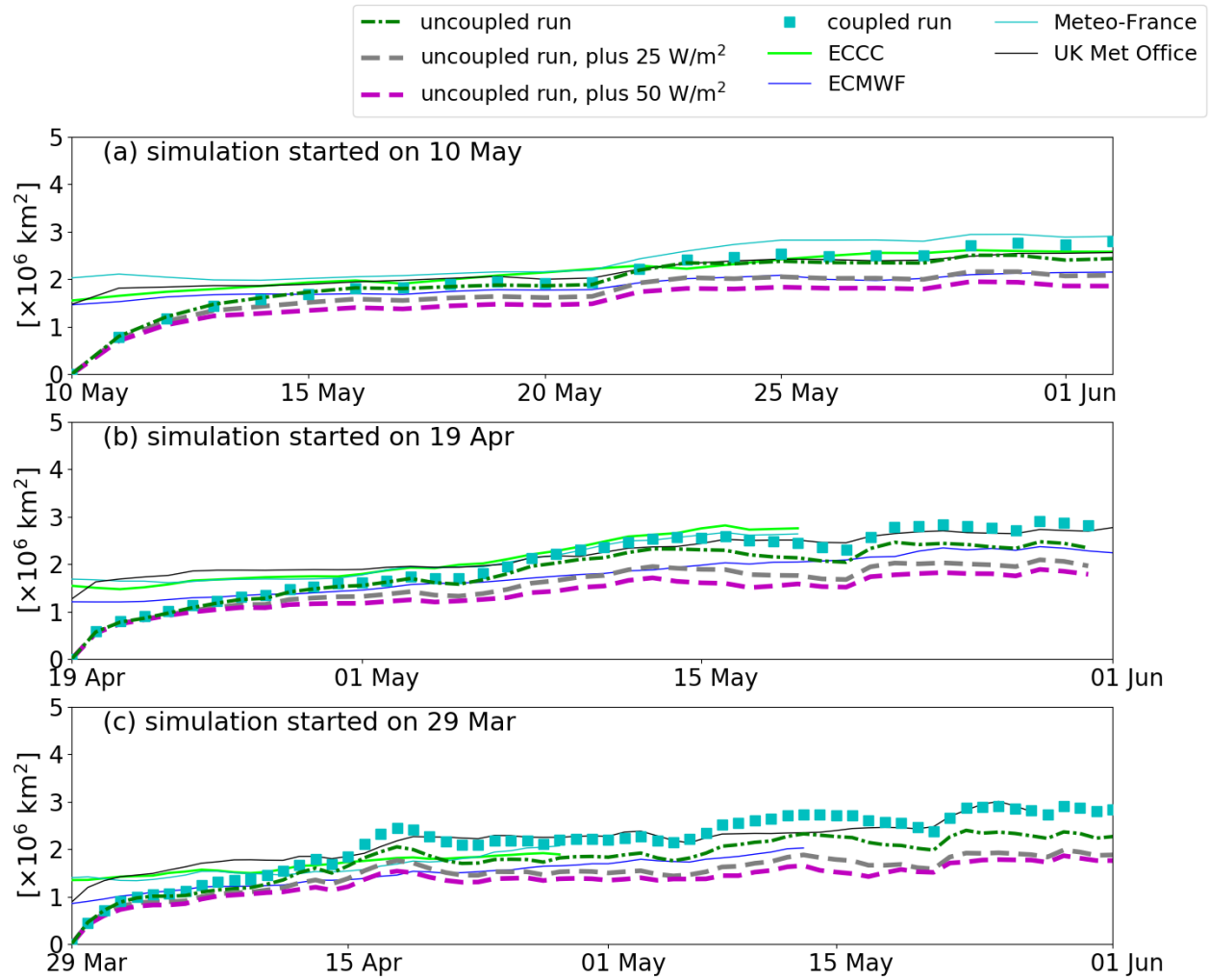
6

Fig. S5. The integrated ice area error, calculated as in Roach *et al* (2020), for the regional MITgcm numerical model (green dot-dashed) uncoupled simulation, (cyan squares) coupled simulation, (gray dashed) uncoupled simulation with an artificial increase of DLW by 25 Wm^{-2}, (magenta dashed) uncoupled simulation with an artificial increase of DLW by 50 Wm^{-2}, and the four forecast systems available from S2S database: (green) ECCC, (blue) ECMWF, (gray) UK Met Office, and (light blue) Météo-France model, for the simulations and S2S forecasts initialized on (a) 10 May, (b) 19 Apr and (c) 29 Mar 2018.

Because the model sea ice fraction was different from the observations (Fig. 7), we additionally examined model bias using a different definition of sea-ice extent, commonly defined by the 15% sea-ice concentration contour. The comparison with the NSIDC data showed that sea ice fraction in the Weddell Sea is more diffuse in our model simulation (Fig. 7); recent in-situ winter observations from the marginal ice zone in the eastern Weddell Sea (Vichi et al 2019) suggest the model results are closer to reality. We compared the sea-ice extent area estimated from our uncoupled model simulation with NSIDC data using the 30% and 50% sea-ice concentration

1   contours (Fig. S8). In all cases, however, the diagnosed sea ice growth in our uncoupled model
2   simulation was faster than in the observations (Fig. S8a). When we made the same comparison for
3   the uncoupled model simulation where we artificially increased the DLW radiation by 50 Wm^{-2},
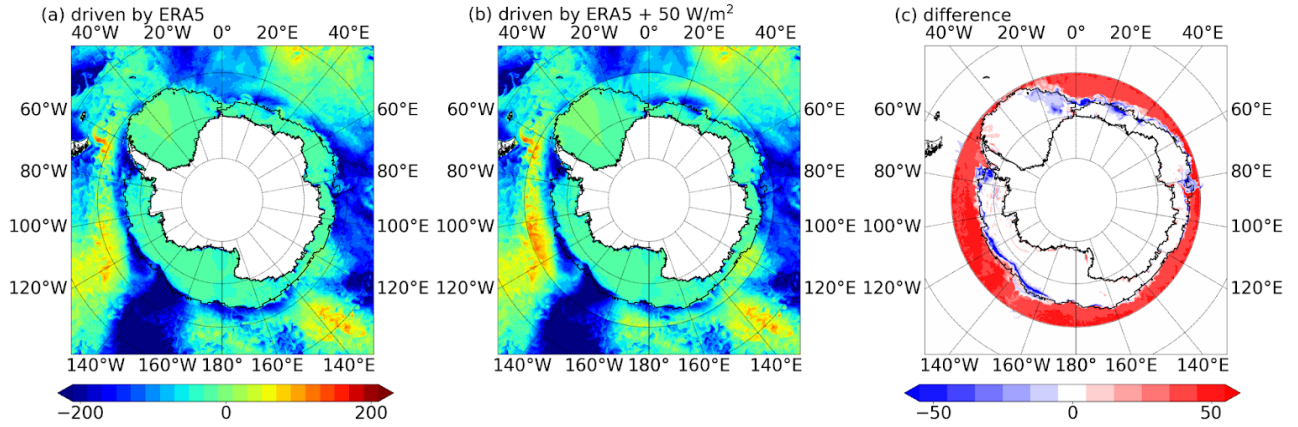4   the comparison was much better for all three definitions of sea-ice extent area (Fig. S8b).

5

6
7
8   Fig. S6. The net surface heat flux Q$_{net}$ from 10 May to 01 Jun 2018 from the MITgcm model driven
9   by (a) ERA5, and (b) ERA5 with an artificial increase of longwave radiation by 50 Wm^{-2}; (c) the
10 difference panel (b) - panel (a). Positive values in panels (a) and (b) indicate the ocean heat gain.
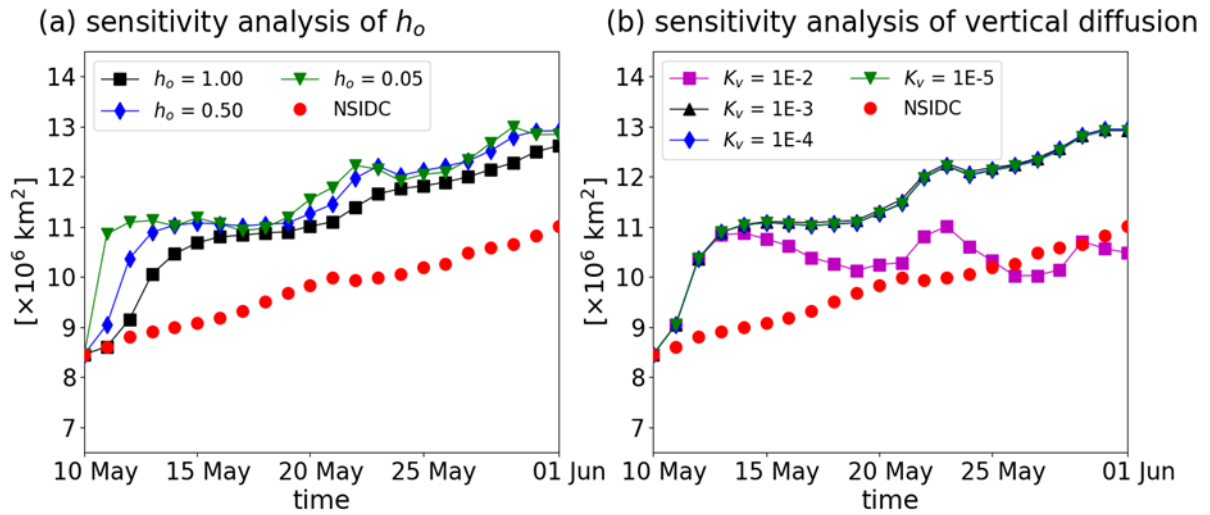11 The contours indicate the sea-ice extent.

12

13
14
15 Fig. S7. The results of the sensitivity analysis of the sea-ice extent area obtained from the
16 uncoupled MITgcm model simulation driven by ERA5. The sea-ice extent area obtained using (a)
17 different lead closing parameter h$_o$ coefficients indicated in the legend, and (b) different vertical
18 diffusivity coefficients indicated in the legend.
19

6. Sensitivity analysis of sea-ice growth to the sea-ice dynamics and albedo

We next carried out a sensitivity analysis of sea-ice growth rate to sea-ice dynamics in the model, running the model with sea ice dynamics on and with sea ice dynamics off (i.e., no sea ice transport). Our sea ice model is a simple one, but this test is informative as the winds in the region of greatest interest (i.e. the northern Weddell Sea) tend to be equatorward (e.g. Fig. 4). Thus ice advection acts to expand the ice cover and omitting ice dynamics all together should represent the end member with the slowest growth attributable to sea ice dynamics. Indeed, turning ice dynamics off reduces the growth, but the impact is less than 10% (Fig. S9a), confirming that the growth in this open-ocean region is primarily due to thermodynamics. Sun and Eisenman (2021) show that modeled biases in long-term sea ice trends can be improved by imposing observed sea ice drift. Consistent with our results, however, they did not find imposing observed drift to robustly [improve seasonal biases. This contrast suggests the long-term sea-ice model biases may be more attributable to dynamics, and seasonal model biases may be more attributable to thermodynamics, though coupling of these components deserves investigation.

Because the albedo is important in parameterizing the sea-ice evolution, we also tested its impact on sea-ice growth in MITgcm. We artificially increased and decreased the albedo by 0.1 from the default values in MITgcm (i.e., dry ice albedo=0.75; wet ice albedo=0.66; dry snow albedo=0.84; wet snow albedo=0.70). The results showed that the sea-ice growth is not sensitive to these changes (Fig. S9b), which is primarily because downwelling shortwave radiation is small in May at these latitudes.

We further tested the sensitivity of sea-ice growth to the perturbations of the initial temperature and salinity. These perturbations (1°C or 1 PSU) are introduced to the ocean model top-level (i.e., upper 4.2 m). The sea-ice evolution is not sensitive to this perturbation of initial temperature (Fig. S10a). Fig. S10b also shows when we add 1 PSU to the initial salinity the sea-ice grows almost as fast as in the control run. However, when we remove 1 PSU the vertical mixing is reduced, and the sea ice grows faster by about 10% compared to the control run.
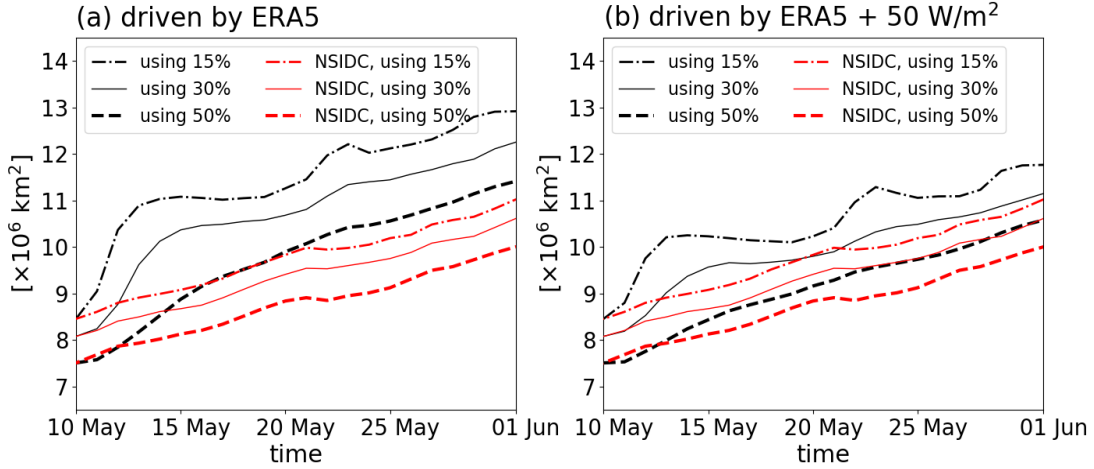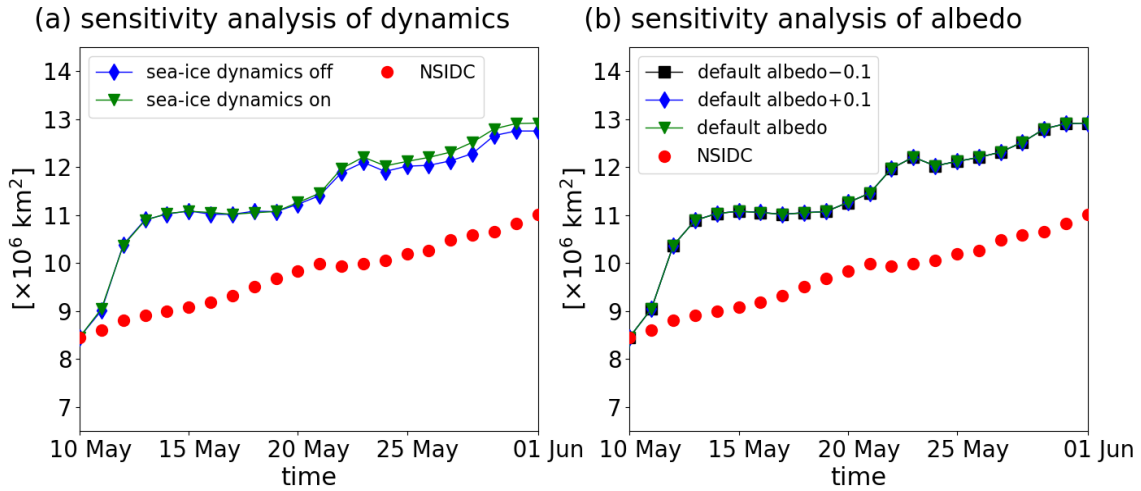
Fig. S8. The comparison of the sea-ice extent area estimated using 15%, 30% and 50% sea-ice concentration contour (as indicated in the legend), obtained from (red) NSIDC observations and (black) uncoupled MITgcm model simulation with (a) ERA5 atmospheric forcing and (b) as panel a, except the DLW radiation was artificially increased by 50 Wm^{-2}.

Fig. S9. The results of the sensitivity analysis of the sea-ice extent area obtained from the uncoupled MITgcm model simulation driven by ERA5. （a）the sensitivity of sea ice to the sea-ice dynamics, （b）the sensitivity of sea ice to different values of albedo used in the model.

(a) sensitivity analysis of perturbed T

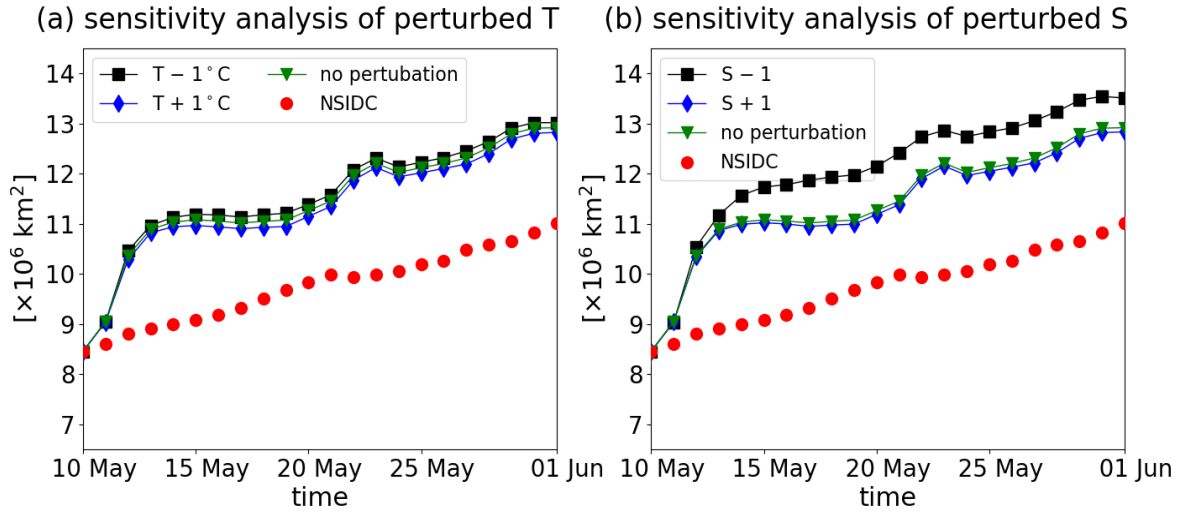**(b) sensitivity analysis of perturbed S**

Fig. S10. The results of the sensitivity analysis of the sea-ice extent area to the perturbation of (a) initial sea surface temperature and (b) sea surface salinity in the MITgcm model.

7. Heat fluxes and MSLP in the coupled model

To test the sensitivity of sea ice evolution in the coupled model due to the heat fluxes, the DLW radiation and the net surface heat flux Q_{net} are shown in Fig. S11 and S12, respectively. It can be seen that the DLW radiation in the coupled model is stronger than the uncoupled run which is driven by ERA5, especially near the Antarctic continent. However, the Q_{net} in the coupled run shows that the ocean does not gain more heat compared with the uncoupled run over the sea ice zone but does over the open ocean to the north. This is a consequence of changes in the coupled model to the other surface heat fluxes, namely turbulent fluxes, emitted longwave radiation, and downward shortwave radiation.

In addition to the heat fluxes, we compare the MSLP obtained from the coupled model in comparison with ERA5. Because we nudged the coupled run to ERA5 throughout most of the Polar WRF model atmosphere, the MSLP in the coupled run agrees well with that in ERA5. The difference is only 1 or 2 hPa in most of the computational domain.
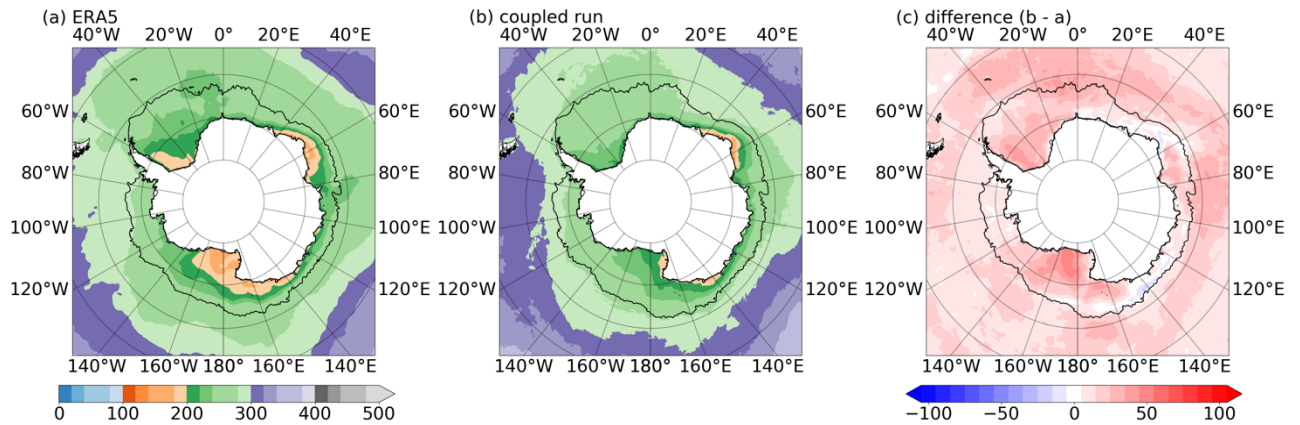
Fig. S11. The DLW radiation from 10 May to 24 May 2018 from the coupled model in comparison with ERA5. The contours indicate the sea-ice extent obtained in the simulations.
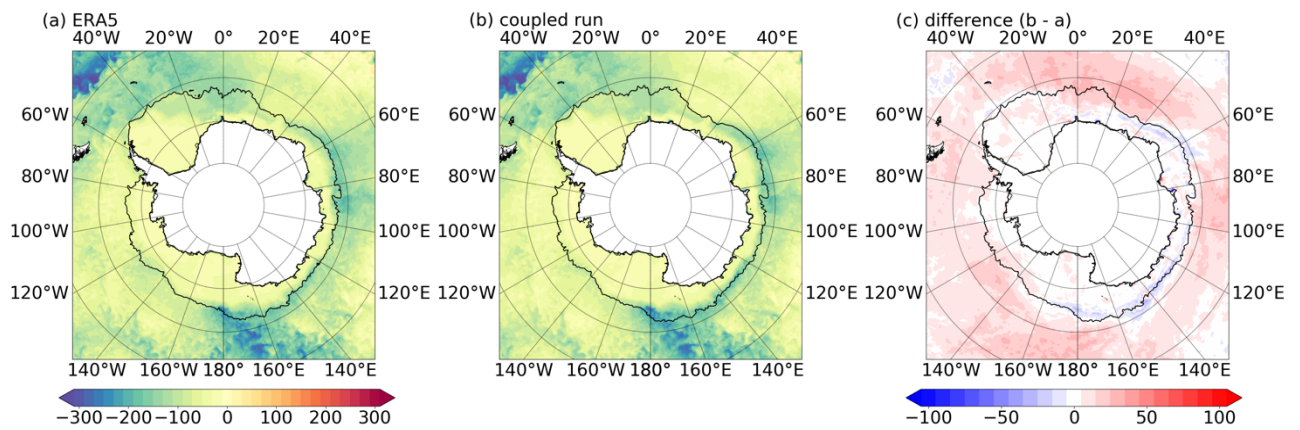

Fig. S12. The time-averaged net surface heat flux Q_{net} from 10 May to 24 May 2018 from the coupled model in comparison with the uncoupled MITgcm model driven by ERA5. In Panels (a-b), positive value indicates the ocean gains heat from the atmosphere. The contours indicate the sea-ice extent obtained in the simulations.

References used solely in Appendix

Chassignet E P, Hurlburt H E, Smedstad O M, Halliwell G R, Hogan P J, Wallcraft A J, Baraille R and Bleck R 2007 The HYCOM (Hybrid Coordinate Ocean Model) data assimilative system *J. Mar. Syst.* **65** 60–83. DOI: 10.1016/j.jmarsys.2005.09.016

Driemel A, and 37 Coauthors, 2018 Baseline Surface Radiation Network (BSRN): structure and data description (1992–2017) *Earth Syst. Sci. Data* **10** 1491–501, https://doi.org/10.5194/essd-10-1491-2018

Hibler W D 1979 A dynamic thermodynamic sea ice model *J. Phys. Oceanogr.* **9** 815–46. https://doi.org/10.1175/1520-0485(1979)009<0815:ADTSIM>2.0.CO;2

Hines K M, Bromwich D H, Wang S, Silber I, Verlinde J and Lubin D 2019 Microphysics of summer clouds in central west Antarctica simulated by Polar Weather Research and Forecasting Model (WRF) and the Antarctic Mesoscale Prediction System (AMPS) *Atmos. Chem. Phys.* **19** 12431-12452, https://doi.org/10.5194/acp-19-12431-2019.

Large W G and Yeager S G 2009 The global climatology of an interannually varying air–sea flux data set *Clim. Dyn.* **33** 341–64. DOI: 10.1007/s00382-008-0441-3

McArthur L J B 2005 *Baseline Surface Radiation Network (BSRN) Operations Manual V2.1*, World Climate Research Programme WMO/TD-no. 1274 ed., WCRP-121.

Morrison H, Curry J A, and Khvorostyanov V I 2005 A new double-moment microphysics scheme for application in cloud and climate models. Part I: Description *J. Atmos. Sci.* **62** 1665–1677, https://doi.org/10.1175/JAS3446.1

Roach L A, Dörr J, Holmes C R, Massonnet F, Blockley E W, Notz D, Rackow T, Raphael M N, O'Farrell S P, Bailey D A and Bitz C M 2020 Antarctic sea ice area in CMIP6. *Geophys. Res. Letts* **47** e2019GL086729. https://doi.org/10.1029/2019GL086729

Sun, S. and Eisenman I. 2021 Observed Antarctic sea ice expansion reproduced in a climate model after correcting biases in sea ice drift velocity. *Nat. Commun.* **12**, 1060. DOI: 10.1038/s41467-021-21412-z

Vichi, M. and 14 Co-authors 2019 Effects of an explosive polar cyclone crossing the Antarctic marginal ice zone. *Geophys. Res. Letts.* **46** 5948–5958. https://doi.org/10.1029/2019GL082457

Wang K and Dickinson R E 2013 Global atmospheric downward longwave radiation at the surface from ground-based observations, satellite retrievals, and reanalyses *Rev. Geophys.* **51** 150–85 https://doi.org/10.1002/rog.20009.